

A New Invasion Model for Resistivity Log Interpretation

A. Q. Howard, Jr.: Schlumberger, Houston, Texas

Abstract: Defining formation resistivity, R_f , is difficult when invasion is deep or the ratio of mud filtrate to connate-water resistivity, R_{mf}/R_w , is extreme. An improvement and automation for this correction is the subject of this paper. The method is based upon multiple-array induction estimates of the radial conductivity profile induced by invasion. Multi-channel induction data, available at each depth, are the key to extending, in a realistic way, the traditional three-parameter invasion model of R_f , R_w , and diameter of invasion, D_i . High vertical resolution and low sensitivity to environmental effects are achieved by a first-step processing of raw array data. Major emphasis is placed on the ability to accurately estimate the formation resistivity, $R_f = 1/\sigma_f$, beyond the invaded zone because this is the quantity that is directly proportional to the volume of hydrocarbon in pay zones.

The radial dependence of the conductivity-model profile is maximally flat and smooth (all order derivatives exist). A simplest example of this type of profile has four parameters, σ_w , σ_f , v , and N , where w is the radius where half of the transition from σ_w to σ_f occurs and N is directly related to the slope of the transition. This choice of profile-type not only increases the accuracy of the true formation-resistivity estimate, R_f , but also prevents spurious overshoots that often occur in least-mean-square estimation methods. In addition, the model avoids known errors in estimating R_f from step-profile models when transition zones are present. The model parameters are computed by minimizing a cost function of the squares of differences between measured and modeled apparent conductivity using a new dynamically constrained Levenberg-Marquardt algorithm. The method is a wellsite product that, because of the multi-channel data base, provides a robust replacement to tornado-chart invasion corrections. In difficult situations where the invasion is deep and/or the dynamic range between R_f and R_w is large, the multi-array data and their processing improve the accuracy of R_f . Results are given for synthetic invaded-bed examples in one and two dimensions. These synthetic results establish the accuracy and robustness of the method. Field-log examples are also given.

INTRODUCTION

This paper offers an improved method of estimating the radial conductivity profile as inferred from many channels of induction data. The input data are acquired by the Array Induction Imager Tool (AIT¹), which has eight balanced three-coil arrays. Because each array measures an R and an X signal, and six arrays operate simultaneously at two frequencies, the tool provides 28

channels of induction data at each depth. Multi-channel induction data are transformed into a parameterized radial conductivity profile that more accurately quantifies the invasion and hence renders an improved R_f estimate.

As compared with the forward problem of predicting the measured voltages for a given borehole, sonde, and formation geometry, this paper deals with the more difficult ill-posed and nonunique problem of attempting to reconstruct the formation two-dimensional conductivity map, given the sonde voltage measurements, and the sonde and borehole geometry. The logging geometry is assumed to be azimuthally symmetric ($\partial/\partial\phi = 0$) with respect to the center of the borehole. If this is not the case, as for example in dipping-bed geometries, the problem is no longer scalar, and because of bed-boundary polarization charges, the apparent conductivity is no longer a linear function of formation conductivity (Howard and Chew, 1992).

In terms of complexity, this approach to the inverse problem lies between strictly one-dimensional thick-bed radial inversion methods and the more ambitious two-dimensional methods. The present method is scalar and only approximately two dimensional. The goal is to develop an approximate solution that fits into the established vertical signal processing reported by Hunka et al. (1990) and Barber and Rosthal (1991). A second goal is estimation of radial conductivity profiles at the wellsite in real time.

Inverse problems in two and three dimensions are computationally intensive, so the second goal places severe restrictions on applicable methods. One of the simplifying features of induction borehole interpretation in the frequency range of 10–100 kHz is the concept of response functions. The concept is valid because the eddy currents induced in the earth in response to the transmitter-coil excitation interact with each other only weakly. Secondary scattering is very small, and the problem is only weakly nonlinear. The dominant manifestation of nonlinearity is the so-called skin-effect, and this is corrected.

The method is based upon multiple array-induction estimates of the radial conductivity profile induced by invasion. The procedure for inverting the array measurements of apparent conductivity for the radial conductivity profiles begins by applying borehole corrections to the raw measurements (Grove and Minerbo, 1991). Next, five linear combinations of the borehole-corrected array measurements are taken over a log interval of several feet. Each of the five resulting processed logs has the

¹ Mark of Schlumberger.

Invasion Model for Resistivity Logs

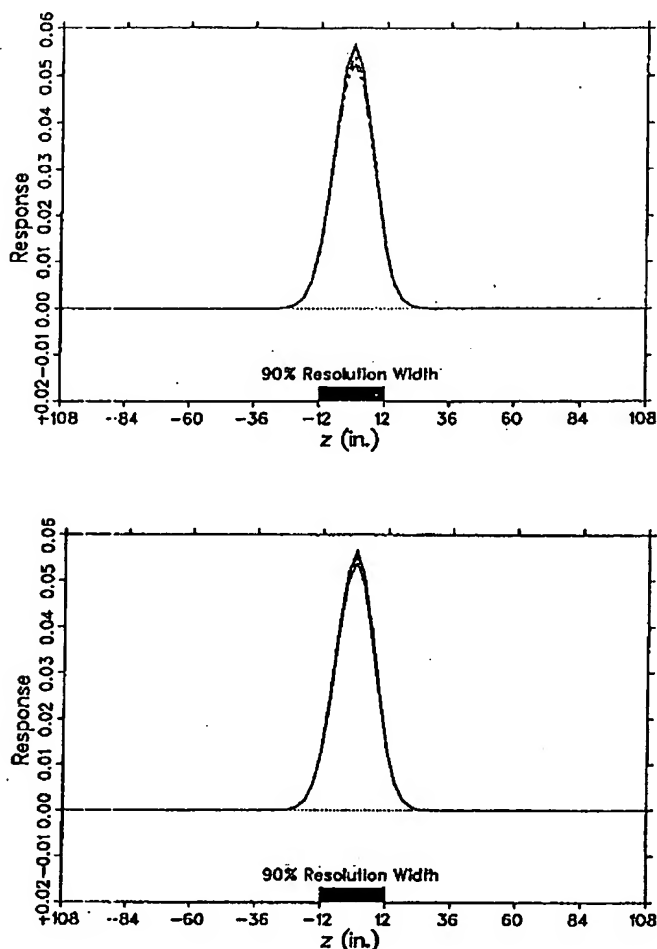


Figure 1: a. Vertical response functions of 10-, 20-, 30-, 60-, and 90-in. median curves at 0 background conductivity. b. 60-in. vertical response function for all background conductivities.

same vertical resolution; median depths of investigation are 10, 20, 30, 60, and 90 in. The weight coefficients that produce these logs are a function of background conductivity and are designed to maintain constant radial and vertical resolution over a wide range of background conductivity. The logs have a tight vertical-invariant focus into the formation independent of formation conductivity. The processed logs have a constant radial median response over the same range of background conductivity. For example, a 30-in. log is produced by formation eddy currents, half of which are inside and half outside of 30 in. The set of five processed log curves is closely vertically matched over narrow depth intervals around vertical step changes in conductivity. The uncertainties associated with vertical bed-boundary effects are minimized. This effectively deconvolves the vertical dimension from the problem except in the immediate vicinity of bed boundaries.

Thus, by design—and prior removal of borehole fields—when the log curves separate, invasion has occurred.

The five processed logs are inverted for the underlying radial conductivity profile. The relationship between the processed logs and the radial conductivity profile is a discretized set of pseudo-radial geometric factors stored on a computer for a range of background conductivities. The radial profile is a four-parameter Butterworth function, which includes a transition region of resistivity with arbitrary inner and outer radii. The four-parameter profile at each depth is obtained using a modified Levenberg-Marquardt (LM) nonlinear iterative solver. The LM algorithm minimizes the weighted sum of least-square differences between the five processed log curves and the model log curves predicted by the four-parameter profiles. The minimum least-mean-square defines the four parameters and hence the radial profile.

An example set of response functions (100 vertical samples) that are linear combinations of all AIT arrays is shown in Figures 1a and 1b. Figure 1a shows that all curves 10, 20, 30, 60, and 90 in. are designed to have the same vertical response. Figure 1b is the vertical response of a 60-in. median filter set for all background conductivities. These two figures demonstrate the degree to which it is possible to focus a fixed vertical response independent of background conductivity. Although not shown, median radial depth of investigation is also maintained. The ability to achieve this invariant and tight focus of the synthesized response is the justification for the decoupling of the radial processing. Details of median curve-filter design are available (Hunka et al., 1990).

PSEUDO-RESPONSE FUNCTIONS

From a measurement point of view, the apparent conductivity of the i th median curve, σ_{ai} , is related through response function theory to the underlying formation by

$$\sigma_{ai} = \sum_{m=1}^{N_R} w_{im} \sigma_m \quad (1)$$

where σ_m is the digitized value of the radial conductivity profile at radius $\rho = \rho_m$, N_R is the number of radial pixels, which is taken to be between 60 and 100 with a 2-in. radial increment, and the weighting function w_{im} is to be determined.

Equation (1) as it stands is not useful for the estimation problem. The complete definitions are lacking, the physics of invasion that determines the shape of the radial profile is not imposed, and the tool physics that relates the response to the formation is missing. The tool physics enters through pseudo-response functions based upon rigorous radial field expansions of Maxwell's equations (Wait, 1984). The concept of pseudo-response functions can be found in Tittman (1986). For this application, note that

Howard

radial conductivity profile containing a single step change in conductivity, $\Delta\sigma$, i.e.,

$$\sigma(\rho) = \sigma_0 + \Delta\sigma u(\rho - \rho_0), \quad (2)$$

defines in a natural way the pseudo-response function $J^j(\rho)$ for the j th induction array ($j = 1, 2, \dots, N_c$) through the apparent-conductivity relation

$$\sigma_a^j = \sigma_{a0}^j + \Delta\sigma \int_0^\infty J^j(\rho) u(\rho - \rho_0) d\rho. \quad (3)$$

Here σ_{a0}^j is the apparent conductivity for formation conductivity σ_0 . Noting that the derivative of the unit step function $u(\rho - \rho_0)$ is the impulse function $\delta(\rho - \rho_0)$, it follows from equation (3) that

$$J^j(\rho) = \frac{1}{\Delta\sigma} \frac{d\sigma_a^j}{d\rho}. \quad (4)$$

For accurate computation of σ_a^j , it is advantageous to define a radial cumulative pseudo-response function $J_c^j(\rho_0)$ as

$$J_c^j(\rho_0) = \int_0^\infty J^j(\rho) d\rho. \quad (5)$$

The advantage of this response function definition is that the area from a fixed radius to infinity is computed accurately as the primary numerical result. Beyond the invaded zone, this is the required quantity to yield optimum σ_a^j estimates. For numerical computation with error of order $(\sigma_{a1} - \sigma_{a2})^2$, a central-difference scheme is used. Thus it is necessary to compute two apparent conductivities, σ_{a1} and σ_{a2} , viz.:

$$\sigma_{a1}^j = \sigma_{a0}^j + \int_0^\infty J^j(\rho)(\sigma_1 - \sigma_0) d\rho, \quad (6a)$$

$$\sigma_{a2}^j = \sigma_{a0}^j + \int_0^\infty J^j(\rho)[\sigma_1 + \Delta\sigma u(\rho - \rho_0) - \sigma_0] d\rho. \quad (6b)$$

The difference of the two equations (6a) and (6b) defines the desired partial cumulative response, i.e.,

$$J_c^j(\rho_0) = \frac{\sigma_{a2}^j - \sigma_{a1}^j}{\Delta\sigma}. \quad (7)$$

Equation (7) is the numerical definition of the pseudo-response function, which is used to compute it given a forward model. Skin correction is accomplished by normalizing response functions to have total unity gain. The definition is

$$K^j(\rho) = J^j(\rho)/N^j(\sigma_0), \quad (8)$$

where

$$N^j(\sigma_0) = \int_0^\infty J^j(\rho) d\rho. \quad (9)$$

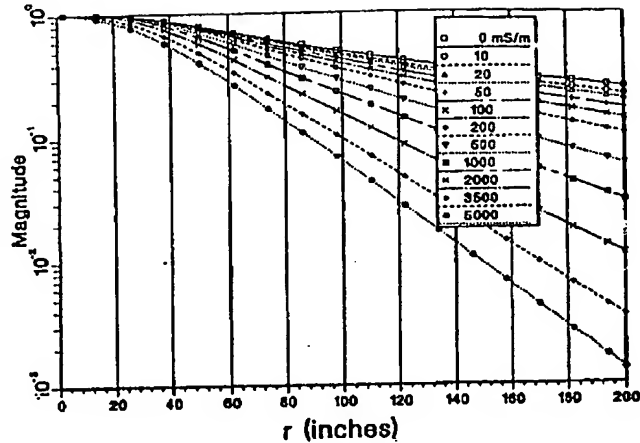


Figure 2: Partial cumulative radial response function $K^j(\rho)$ as defined by equation (8) for deep reading array and background conductivities, as shown in legend.

Note that $N^j = J_c^j(0)$. An example normalized partial-cumulative radial-response function computed by equation (8) for a deep-reading array is given in Figure 2. In the next section, the pseudo-response function will be used to deconvolve the formation conductivity. In the appendix, analytic forms of the normalization function are given for both the dipole and more general loop cases.

RADIAL DECONVOLUTION

In this section, it is assumed that the formation resistivity varies only radially. Using the response functions defined in the previous section, the apparent conductivity measured by the j th channel is simply

$$\sigma_a^j = \int_0^\infty K^j(\rho)\sigma(\rho) d\rho. \quad (10)$$

For numerical purposes, it is convenient to define the radial conductivity profile $\sigma(\rho)$ as the finite-element model

$$\sigma(\rho) = \sum_{m=0}^{N_R} \sigma_m \Delta_m(\rho) + \sigma_{N_R} u(\rho - \rho_{N_R}). \quad (11)$$

In equation (11), $\Delta_m(\rho)$ is the m th triangular finite element defined as

$$\Delta_m(\rho) = \begin{cases} 1 - |\rho - \rho_m|/\Delta_m, & \text{if } \rho_{m-1} < \rho < \rho_m; \\ 1 - |\rho - \rho_m|/\Delta_{m+1}, & \text{if } \rho_m < \rho < \rho_{m+1}; \\ 0, & \text{otherwise.} \end{cases} \quad (12)$$

where $m = 1, 2, \dots, N_R - 1$, $\Delta_m = \rho_m - \rho_{m-1}$, and $\rho_0 = 0$. Note in equation (10) that because of the normalization of the kernel functions, K^j , it is not necessary to include an explicit additive background conductivity. Note also that the ρ axis subdivision need not be uniform, it is only

Invasion Model for Resistivity Logs

necessary that it be ordered, $\rho_0 < \rho_1 < \dots < \rho_{N_R}$. The first and last triangular functions are special cases given by

$$\Lambda_0(\rho) = \begin{cases} 1 - |\rho - \rho_0|/\Delta_1, & \text{if } \rho_0 < \rho < \rho_1; \\ 0, & \text{otherwise.} \end{cases} \quad (13)$$

$$\Lambda_{N_R}(\rho) = \begin{cases} 1 - |\rho - \rho_{N_R}|/\Delta_{N_R}, & \text{if } \rho_{N_R-1} < \rho < \rho_{N_R}; \\ 0, & \text{otherwise.} \end{cases} \quad (14)$$

The linear combination of the triangular functions in equation (11) yields a piecewise linear function over the entire finite-element interval (ρ_0, ρ_{N_R}) and hence yields a higher-order expansion than one with piecewise constant elements. Beyond ρ_{N_R} the unit step function in equation (11) forces the profile to the constant ρ_{N_R} . Substitution of equation (11) into equation (10) yields

$$\sigma_a^j = \sum_{m=1}^{N_R} P_m^j \sigma_m \quad (15)$$

where

$$P_m^j = \int_{\rho_{m-1}}^{\rho_{m+1}} \Lambda_m(\rho) K(\rho) d\rho. \quad (16)$$

The finite-element matrix P_m^j can be written in terms of partial radial-response functions defined by equation (7), i.e., let

$$G_m^j = J_m^j(\rho_m)/N^j(\sigma_0). \quad (17)$$

Then the finite-element matrix P_m^j has the explicit representation

$$P_m^j = \begin{cases} (1 - G_1^j)/2, & \text{if } m = 0; \\ (G_{m-1}^j - G_{m+1}^j)/2, & \text{if } 0 < m < N_R; \\ (G_{N_R-1}^j + G_{N_R}^j)/2, & \text{if } m = N_R. \end{cases} \quad (18)$$

The partial cumulative response functions $G_m^j(\sigma_0)$ are computed and stored in table form on computer disk. The table consists of uniform 2-in. steps from 2 to 200 in. ($m = 1, 2, \dots, 100$) for each array ($j = 1, 2, \dots, 28$) and background conductivities $\sigma_0 = 0, 0.01, 0.02, 0.05, 0.1, 0.2, 0.5, 1, 2, 3.5$, and 5 S/m. A check on the normalization is made by choosing $\sigma_m = \sigma_c$ for all m . Then all curves should read the correct homogeneous value σ_c .

$$\begin{aligned} \sigma_a^j &= \sum_{m=1}^{N_R} P_m^j \sigma_m \\ &= \sigma_c \sum_{m=1}^{N_R} P_m^j \\ &= \sigma_c (1 + G_0^j)/2, \\ &= \sigma_c \end{aligned} \quad (19)$$

In equation (19), the fact $G_0^j = 1$, which follows from equation (8), is needed. As an example of the response

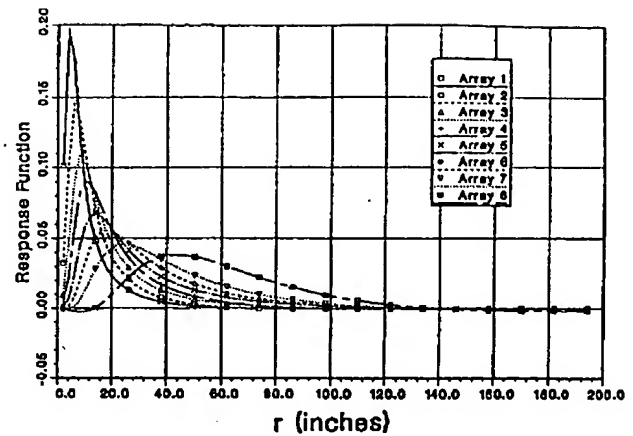


Figure 3: Real part of differential radial response functions for all arrays defined by finite element matrix $P_m^j(\sigma_0)$ for $\sigma_0 = 1$ S/m (see equation [16]). The response function is based upon triangular finite-element shape functions $\Lambda_m(\rho)$.

functions, P_m^j , the matrix is shown in Figure 3 for background of 1 S/m for all arrays j . The legend labels raw array responses 1–8 in order of increasing depth of investigation. The abscissa is m converted to inches. An important point illustrated by Figure 3 is that it is more difficult to focus the response radially beyond about 30–50 in. than it is to focus the response vertically because the focus is achieved in the static limit of Maxwell's equations rather than by interference effects that are responsible for high resolution in microwave imaging where the size of the narrow beam-forming antennas is more than 1 wavelength. Microwave imaging intrinsically allows much higher resolution as the distance from the source is increased. In high-loss media, as encountered in well logging, skin-effect is not negligible, and it is necessary to use induction methods. Then the ability to focus the quasi-static field is based upon the much more difficult and limited ability to shape near-field source singularities. This ability degrades rapidly as one moves away from the borehole, as is evident in Figure 3.

As discussed in the introduction, the primary measurements are combined to produce focused apparent-conductivity median logs. Median logs in the case of thick beds are produced by linear combinations of the primary measurements of the form

$$\sigma_{ai} = \sum_{j=1}^{N_c} \tilde{w}_j(\sigma_0) \sigma_a^j \quad (20)$$

The index j is reserved for actual sonde data, and the index i is associated with the processed or median curves. The weights $\tilde{w}_j(\sigma_0)$ produce a focused log with median depths of investigation of 10, 20, 30, 60, and 90 in., as $i = 1, 2, 3, 4$, and 5 . The weights are designed to have identical step responses for all curves (i) and background

Howard

conductivity. In addition they are normalized such that

$$\sum_{j=1}^{N_c} \tilde{w}_j(\sigma_0) = 1. \quad (21)$$

The focusing-weights design is treated by Barber and Rosenthal (1991). It is important to note that the dependence on the vertical-focusing property of the weights $\tilde{w}_j(\sigma_0)$ is implicit; the filter weights, which produce the median curves from the multi-channel sonde data, are summed over the vertical index (along the log axis) to produce $\tilde{w}_j(\sigma_0)$. Combining equations (15) and (20) results in

$$\sigma_{ai} = \sum_{m=0}^{N_r} w_{im}(\sigma_0) \sigma_m, \quad (22)$$

where $i = 1, 2, \dots, M_c$. Note equation (22) is equation (1), but where now the weight matrix $w_{im}(\sigma_0)$ is

$$w_{im}(\sigma_0) = \sum_{j=1}^{N_c} \tilde{w}_j(\sigma_0) F_m^j(\sigma_0), \quad (23)$$

where $F_m^j(\sigma_0)$ are the tabulated radial-response functions given by equation (18). This completes the description of the input curves σ_{ai} , which are the starting points for the estimation of the radial conductivity profile.

PARAMETRIC PROFILES

The shape of the invasion profile is determined by the mixture of connate water, mud filtrate, and hydrocarbon in the pore space of formation rock. Wireline-induction measurements are usually taken several hours to days after the hole is drilled. When the formation is water wet, after the oil phase has a higher relative permeability. If the formation water is more conductive than the mud filtrate, the transition region will have an excess of formation water resulting in a conductive annulus (Broussard, 1989). Depending on the annulus thickness, conductivity contrast, and distance from the well bore, the electric measurement may or may not be sensitive to the presence of the annulus.

If several independent channels of induction data are available, it is possible and desirable to go beyond the traditional three-parameter profile of flushed-zone resistivity, R_{xo} , formation resistivity, R_i , and diameter of invasion, D_i . (The question of the number of independent induction channels can be determined by an eigen analysis of a matrix whose rows are a discrete version of the radial response function for each channel.) It also is desirable to have the parameters part of the wellsite presentation. With five induction curves, it is feasible, although not necessarily possible, to resolve four parameters because four curves could be equal to within noise. This is the situation in shales and tight rocks.

Invasion of wellbore fluid into permeable formations produces a radial conductivity profile. Unless the formation rock is almost impermeable, <10 md, the invasion is controlled by the mudcake formed at the borehole wall (Allen, 1991). The shape of the invasion profile in wall (Allen, 1991). The shape of the invasion profile in the transition region, where the resistivity varies from R_{xo} to R_i , depends in a complicated way on relative permeabilities, the ratio R_{mf}/R_w , and pore-space geometry. Formation heterogeneities cause fluid fingering that, when averaged around the wellbore by a mandrel resistivity sonde, smear out the invasion front. By definition, the flushed region, if it exists, will have zero slope radially, as does the noninvaded zone associated with R_i . A four-parameter profile having these properties is the maximally flat profile. In electronic-filter design theory, this function is the Butterworth filter (Oppenheim and Schaffer, 1975). For this application, given in conductivity units (S/m), the function is

$$\sigma_4(\rho) = \sigma_i + (\sigma_{xo} - \sigma_i) / [1 + (\rho/w)^N]. \quad (24)$$

The profile $\sigma_4(\rho)$ has four parameters. In the original filter design application, the order of the filter N is required to be a positive integer to have a passive realization. Here it is only necessary for N to be positive. Notice the distance w is the halfway point of the transition between σ_{xo} and σ_i . Some examples of the Butterworth profile are given in Figures 4–6. The profiles are maximally flat in the flushed zone because when N is a positive integer, the first $N - 1$ derivatives of the profile $\sigma_4(\rho)$ with respect to ρ are zero at $\rho = 0$. Note also that in the limit of large N , the profile $\sigma_4(\rho)$ approaches the traditional three-parameter σ_{xo} , σ_i , D_i profile upon which the tornado-chart interpretation is based. For transition-zone interpretation, two derived distances, r_1 and r_2 , define, respectively, the end of the flushed zone and the beginning of the noninvaded zone.

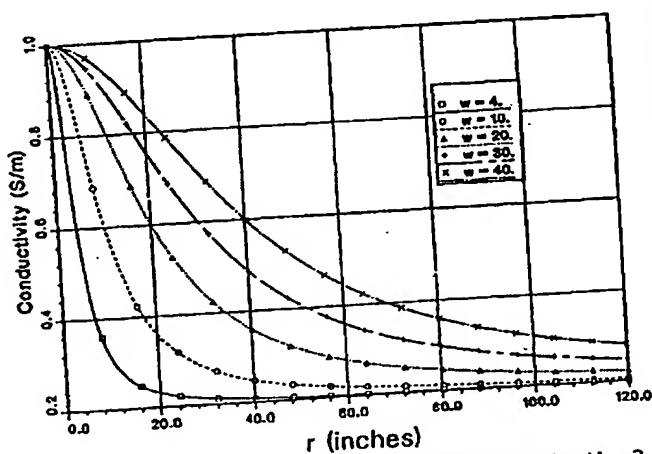
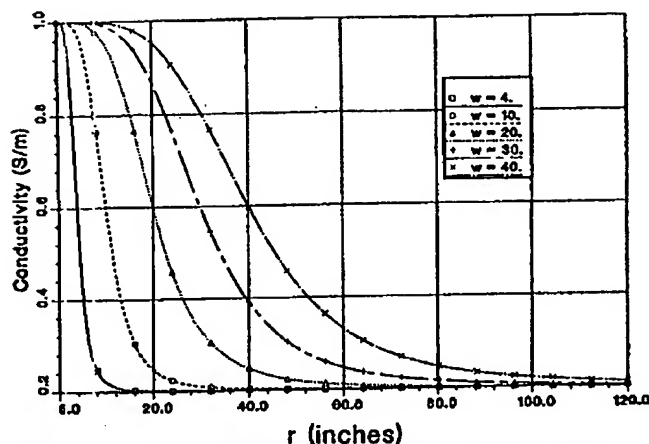


Figure 4: Four-parameter maximally flat profiles for $N = 2$.

March–April, 1992.

The Log Analyst

Invasion Model for Resistivity Logs

Figure 5: Four-parameter maximally flat profiles for $N = 4$.

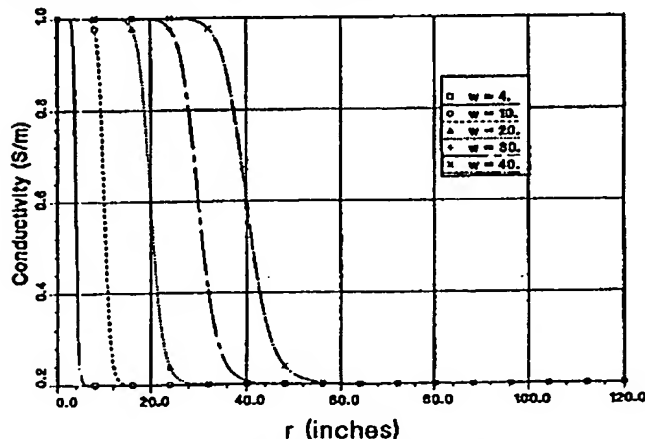
$$\begin{aligned} r_1 &= w(1 - 2/N), \\ r_2 &= w(1 + 2/N). \end{aligned} \quad (25)$$

Radii r_1 and r_2 are defined as the intersections of straight lines associated with, respectively, the inner and outer horizontal asymptotes, and the line passing through the midpoint (w , $[\sigma_i - \sigma_{xo}]/2$) and tangent to the profile at the same point. The order parameter N , which is proportional to the slope of the transition, and the midpoint transition radius w are nonlinear parameters, whereas the asymptotes σ_{xo} and σ_i are linear parameters of the maximally flat model.

The parametric profile can easily be extended to allow for an annulus. As an example, a six-parameter profile $\sigma_6(\rho)$ with three conductivity parameters σ_{xo} , σ_{an} , σ_i , two transition radii, w_1 , w_2 (where $0 < w_1 < w_2$), and one slope parameter N is

$$\sigma_6(\rho) = \sigma_i + (\sigma_{xo} - \sigma_{an})f(\rho, w_1, N) + (\sigma_{an} - \sigma_i)f(\rho, w_2, N), \quad (26)$$

where $f(\rho, w, N) = 1/[1 + (\rho/w)^N]$.

Figure 6: Four-parameter maximally flat profiles for $N = 16$.

The limit of large N is an important limiting case that allows the identification of the significance of the three conductivities appearing in equation (26). Then equation (26) reduces to a rectangular step profile, i.e.,

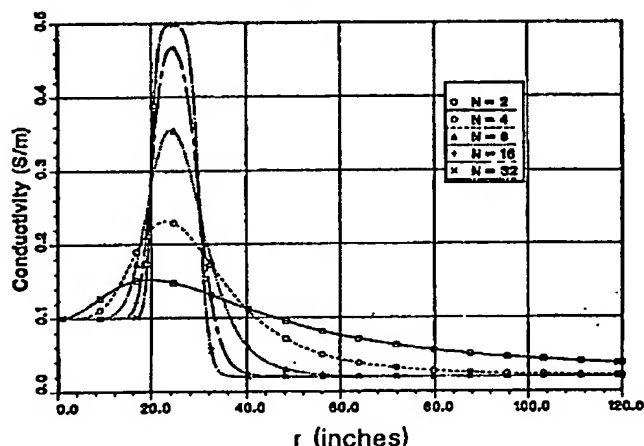
$$\lim_{N \rightarrow \infty} \sigma_6(\rho) = \begin{cases} \sigma_{xo}, & \text{if } 0 \leq \rho \leq w_1; \\ \sigma_{an}, & \text{if } w_1 \leq \rho \leq w_2; \\ \sigma_i, & \text{if } \rho \geq w_2. \end{cases} \quad (27)$$

An example $\sigma_6(\rho)$ profile with $w_1 = 20$ and $w_2 = 30$ is given in Figure 7 for several values of N as indicated in the legend. The four-parameter method developed in this paper could apply equally well to profiles given by equations (24) and (26) or any number of radial regions. The fundamental limitation is the ability of induction data to resolve more than perhaps six parameters.

NONLINEAR PARAMETER ESTIMATION

The parametric conductivity profile model is nonlinear in the transition radius w and the order N . Thus a nonlinear estimation method is required. The method of choice, resulting from work with several methods, is a modified LM algorithm adapted from *Numerical recipes* (Press et al., 1986). The idea is to match the apparent-conductivity log data σ_{ai} with maximally flat model-based estimates $\hat{\sigma}_{ai}(m)$ (see equation [22]) for the $i = 1, 2, \dots, M_c$ by adjusting the formation conductivity profile. The hat notation of statistical estimation theory denotes an estimate. The argument m of the estimate is the estimated model vector whose components in the case of a four-parameter profile are given by

$$\begin{aligned} m_1 &= \hat{\sigma}_{xo}, \\ m_2 &= \hat{\sigma}_{an}, \\ m_3 &= \hat{w}, \\ m_4 &= \hat{N}. \end{aligned} \quad (28)$$

Figure 7: Six-parameter maximally flat profiles with conductive annulus with break points of $w_1 = 20$ and $w_2 = 30$ in.

Howard

The estimation method does not depend upon the specific number of measurements, M_c , or model parameters, N_p . Of course, how well the method performs does depend on M_c and N_p . The model parameters enter through the radial pixel estimates $\hat{\sigma}_m$ of the formation conductivity. From equation (23), the relation is

$$\hat{\sigma}_{ai}(m) = \sum_{m=0}^{N_c} w_{im}(\sigma_0) \hat{\sigma}_m \quad (29)$$

where $\hat{\sigma}_m = \sigma_{N_p}(\rho_m)$.

In equation (29), $\sigma_{N_p}(\rho)$ is an N_p parameter maximally flat profile such as equations (24) or (26), and ρ_m is a member of the discretization of the ρ axis as defined between equations (12) and (13). In the usual application of the LM algorithm, and in terms of these definitions, the model vector \mathbf{m} is the vector that minimizes the χ^2 fit to the data. The definition is

$$\chi^2(\mathbf{m}) = \sum_{i=1}^{M_c} |[\sigma_{ai} - \hat{\sigma}_{ai}(\mathbf{m})]/\sigma_i|^2, \quad (30)$$

where σ_{ai} is the i th input median apparent-conductivity data channel. The conductivity σ_i is the associated standard deviation of the i th data channel and is an a-priori estimate of the reliability of the data; alternatively σ_i can represent the ability of the underlying model for the radial conductivity profile to fit the actual profile.

The method requires knowledge of the gradient (first derivative) and the second partial derivative matrix (Hessian matrix) of $\chi^2(\mathbf{m})$ with respect to the model vector \mathbf{m} . The goodness of fit $\chi^2(\mathbf{m})$ is approximated by a quadratic surface in the model parameters m_k

$$\chi^2(\mathbf{m}) = \gamma - \beta \cdot \mathbf{m} + \frac{1}{2} \mathbf{m} \cdot \mathbf{H} \cdot \mathbf{m} + \dots \quad (31)$$

A necessary condition for the minimum $\mathbf{m} = \mathbf{m}_0$ of $\chi^2(\mathbf{m})$ is that the gradient with respect to the model parameters be zero:

$$\nabla \chi^2(\mathbf{m}) = 0, \quad (32)$$

which from equation (31) yields the condition

$$\mathbf{H} \cdot \mathbf{m}_0 = \beta. \quad (33)$$

An iterative equation for the minimum is found by setting the gradient of equation (31) to zero and then substituting β from equation (33) into the result to obtain the iterative solution

$$\mathbf{m}_{new} = \mathbf{m}_{old} + \mathbf{H}^{-1}[-\nabla \chi^2(\mathbf{m}_{old})]. \quad (34)$$

As it stands, equation (34) is not suitable. Near the minimum it has quadratic convergence but may fail to find the minimum unless the initial estimate is close enough. In addition, the Hessian matrix \mathbf{H} can be singular or ill conditioned. The LM algorithm cleverly overcomes

these deficiencies by adding a numerical parameter λ , which improves the conditioning problem. It also enables the iterative procedure to alternate between a gradient search when the current model estimate \mathbf{m} is far from the minimum, and therefore approximation (31) is not applicable, and a quadratic convergence solution approaching equation (34) near the minimum. The LM algorithm iteratively solves the modified system

$$\mathbf{m}_{new} = \mathbf{m}_{old} + \mathbf{L}^{-1}[-\nabla \chi^2(\mathbf{m}_{old})], \quad (35)$$

where

$$\mathbf{L}_{nm} = (1 + \lambda \delta_{nm}) \mathbf{H}_{nm}, \quad (36)$$

and where δ_{nm} is the Kronecker delta, which is 1 if $n = m$ and zero otherwise. When λ is small, equation (35) reverts to equation (34), which is appropriate near the minimum. However when λ is large, the matrix \mathbf{L} and its inverse become diagonal. In this limit, equation (35) becomes a gradient method that chooses a new estimate model vector, \mathbf{m}_{new} , to be downhill from the previous estimate, \mathbf{m}_{old} . The algorithm contains a loop that solves equation (35). After each iteration, $\chi^2(\mathbf{m}_{new})$ is compared with $\chi^2(\mathbf{m}_{old})$. If it is smaller, λ is decreased by a factor of 10, otherwise it increases λ by a factor of 10. Then \mathbf{m}_{old} is set equal to \mathbf{m}_{new} , and iteration continues until convergence is achieved. A more explicit form of equation (34) is found by computing the gradient and Hessian matrix from equation (30). The results are

$$\begin{aligned} -[\nabla \chi^2(\mathbf{m})]_k &= 2 \sum_{i=1}^{M_c} \frac{[\sigma_{ai} - \hat{\sigma}_{ai}(\mathbf{m})]}{\sigma_i^2} \frac{\partial \hat{\sigma}_{ai}(\mathbf{m})}{\partial m_k}, \\ &\equiv 2\beta_k, \\ \frac{\partial^2 \chi^2(\mathbf{m})}{\partial m_k \partial m_l} &= 2 \sum_{i=1}^{M_c} \frac{[\sigma_{ai} - \hat{\sigma}_{ai}(\mathbf{m})]}{\sigma_i^2} \frac{\partial^2 \hat{\sigma}_{ai}(\mathbf{m})}{\partial m_k \partial m_l} \\ &\quad - 2 \sum_{i=1}^{M_c} \frac{1}{\sigma_i^2} \frac{\partial \hat{\sigma}_{ai}(\mathbf{m})}{\partial m_k} \frac{\partial \hat{\sigma}_{ai}(\mathbf{m})}{\partial m_l}, \\ &\equiv 2\mathbf{H}_{kl}. \end{aligned} \quad (37)$$

Define the change in the model vector as

$$\delta \mathbf{m} = \mathbf{m}_{new} - \mathbf{m}_{old}. \quad (38)$$

Then the matrix equation (35) has the more explicit form

$$\sum_{l=1}^{N_p} \mathbf{L}_{kl} \delta m_l = \beta_k. \quad (39)$$

For cases of deep invasion ($w > 30$), the induction measurement is not sensitive to the shape of the formation conductivity profile controlled by model parameter N as can be determined by examining the response functions defined by equation (5). Another poorly resolved case occurs in tight rocks, where the radial profile can be

Invasion Model for Resistivity Logs

featureless. In such cases, which often occur, matrix equation (39) is poorly conditioned and sometimes singular. In least-square estimation methods, the system matrix is often modified to improve its condition by adding a constraint matrix such as minimum energy or curvature. Twomey (1977) gives several examples showing the solution enhancement possible by conditioning. If the system is linear, the optimum least-square method with minimum norm solution is obtained by singular value decomposition.

For linear systems, certain classes of constraint yield a unique solution to the model vector \mathbf{m} . In the case of minimum energy, uniqueness can be proven (Howard et al., 1983). Uniqueness occurs because the conditioned system matrix can be shown to be nonsingular. As a further benefit, conditioned methods are a means to apply additional physical constraints on the model vector \mathbf{m} . The LM problem is nonlinear and has a special χ^2 structure, so dynamically constrained LM (DCLM) is an extension of the method. For the induction problem, a simple but effective constraint modification of LM results from appending a dummy data channel to the χ^2 variable, i.e.,

$$\chi^2(\mathbf{m}) = \chi_0^2(\mathbf{m}) + C(\mathbf{m}), \quad (40)$$

where the constraint $C(\mathbf{m})$ is chosen to be a simple quadratic form in the model parameters

$$C(\mathbf{m}) = |[\sigma_{aN_c+1} - \hat{\sigma}_{aN_c+1}(\mathbf{m})]/\sigma_{N_c+1}|^2, \quad (41)$$

where

$$\hat{\sigma}_{aN_c+1}(\mathbf{m}) = \sum_{k=1}^{N_p} [(m_k - m_{0k})/\sigma_{mk}]^2, \\ \sigma_{aN_c+1} = 0.$$

The constraint tends to keep the four parameters (see equation [28]) in reasonable ranges

$$-\sigma_{mk} + m_{0k} < m_k < \sigma_{mk} + m_{0k}, \quad (42)$$

for $k = 1, 2, \dots, N_p$. An important additional hard constraint for this profile estimation problem is that all parameters are positive. Because the LM method is nonlinear, positivity is guaranteed by the change of model variables

$$m_k = q_k^2, \quad (43)$$

which modifies matrix equation (39):

$$\sum_{i=1}^{N_p} \mathbf{L}'_{ki} \delta q_i = \beta'_k, \quad (44)$$

where

$$\mathbf{L}'_{ki} = 4q_k q_i (1 + \delta_{ki} \mathbf{H}_{ki}), \\ \beta'_k = 2q_k \beta_k,$$

and where \mathbf{H}_{ki} and β_k are given by equation (37). The relative emphasis of the solution on the constraint $C(\mathbf{m})$ is determined by σ_{N_c+1} . It is not possible to predict (within an order of magnitude) the model data fit $\chi_0^2(\mathbf{m})$ achieved on an arbitrary input data set. This observation motivates the dynamic adjustment of σ_{aN_c+1} . The dynamic adjustment of the constraint weight attempts to keep each matrix equation in the nonlinear iteration method well conditioned. In the process of convergence, the data-dependent term $\chi_0^2(\mathbf{m})$ gradually, iteration by iteration, becomes smaller by several orders of magnitude. For a good solution during the iteration, it is necessary for the conditioning to become smaller at the same rate. This is an additional complication compared to linear conditioned estimation. The DCLM algorithm also deals with cases where the model may not fit the data and smoothly tracks a minimum χ^2 solution into poorly conditioned parameter regimes.

Dynamic conditioning results by choosing σ_{N_c+1} such that the relative weight of the constraint σ_{aN_c+1} to model data fit $\chi_0^2(\mathbf{m})$ ratio is kept at a constant value γ

$$C(\mathbf{m})/\chi_0^2(\mathbf{m}) = \gamma. \quad (45)$$

The DCLM iteration path to the minimum χ^2 solution can go through regions of large condition number c_N of the matrix \mathbf{L}'_{ki} defined by equation (44). In general too, the problem is ill conditioned, so that the choice of matrix algorithm for solving equation (44) is critical. Good matrix algorithms for this purpose are Linpack (Dongarra et al., 1979) double-precision symmetric indefinite factorization, DSICO, and solver, DSISL (which also report the condition number).

In summary, the new DCLM-algorithm iteration scheme is 1) initialize parameter vector \mathbf{m} ; 2) solve equation (44) for the new model parameters \mathbf{m}_{new} ; 3) determine the relative-constraint weighting numerical parameter σ_{N_c+1} according to equation (45), where σ_{N_c+1} is defined by equation (41) (in the numerical results to follow, the ratio parameter γ is chosen to be $1/4$); and 4) check results to determine if the solution has converged, and if not, repeat the iteration.

NUMERICAL RESULTS

Several cases of invasion profiles in thick beds are shown in Figures 8–15. In each of these, the upper half of the figure is the result plotted in log resistivity ($\log_{10}[R]$), where $R = 1/\sigma$ is in ohm-m. The same data are plotted in the lower half of the figure with a linear conductivity σ scale in mS/m. The abscissa is the radial coordinate r between the borehole radius and 120 in. Of the two equivalent representations, the conductivity is actually computed and more closely reflects the sensitivity of the measurement.

Howard

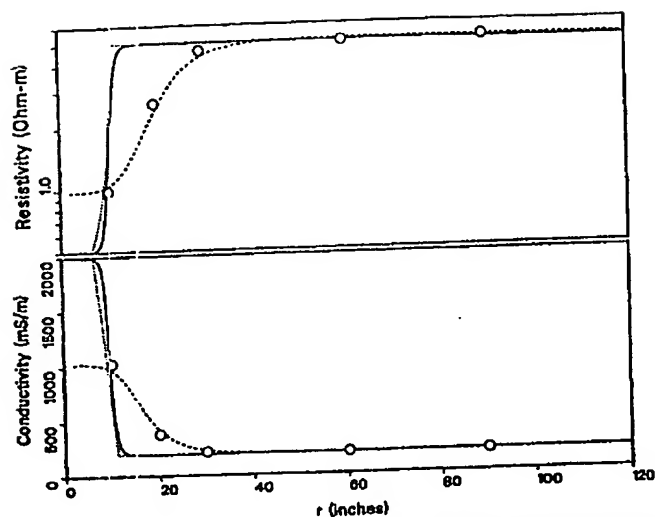


Figure 8: Thick-bed simulation where large dots are median curves, dotted line is model formation, dashed line is initial estimate, and solid line is DCLM estimate for $\chi_0^2 = 1.09 \times 10^0$, $c_N = 7.56 \times 10^3$, $N = 16.1$, $w = 9.5$, and iterations = 59.

	r_1 (in.)	r_2 (in.)	σ_r (mS/m)	σ_{∞} (mS/m)
model	6.50	11.50	200.0	2,000.0
estimate	9.1	10.7	200.6	1,988.0

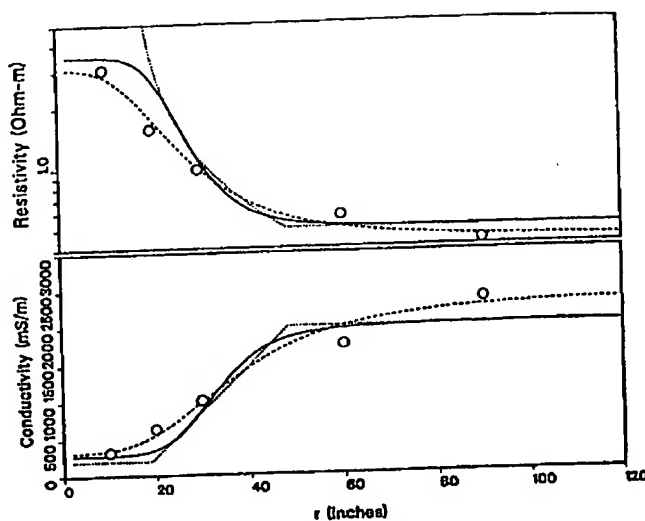


Figure 10: Thick-bed simulation where large dots are median curves, dotted line is model formation, dashed line is initial estimate, and solid line is DCLM estimate for $\chi_0^2 = 2.08 \times 10^{-1}$, $c_N = 2.25 \times 10^3$, $N = 6.0$, $w = 33.2$, and interactions = 24.

	r_1 (in.)	r_2 (in.)	σ_r (mS/m)	σ_{∞} (mS/m)
model	19.0	49.0	2,000.0	200.0
estimate	22.2	44.2	2,007.0	283.2

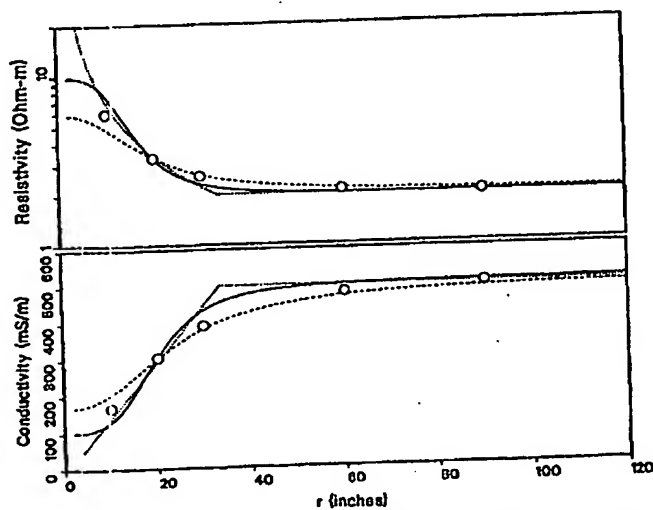


Figure 9: Thick-bed simulation where large dots are median curves, dotted line is model formation, dashed line is initial estimate, and solid line is DCLM estimate for $\chi_0^2 = 4.64 \times 10^{-4}$, $c_N = 5.85 \times 10^3$, $N = 3.69$, $w = 19.9$, and iterations = 26.

	r_1 (in.)	r_2 (in.)	σ_r (mS/m)	σ_{∞} (mS/m)
model	4.0	34.0	500.0	50.9
estimate	8.3	30.7	506.7	101.2

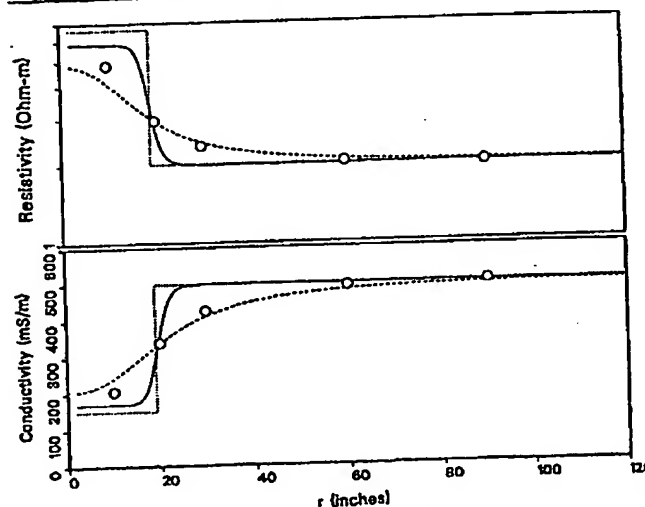


Figure 11: Thick-bed simulation where large dots are median curves, dotted line is model formation, dashed line is initial estimate, and solid line is DCLM estimate for $\chi_0^2 = 1.60 \times 10^{-2}$, $c_N = 1.13 \times 10^4$, $N = 15.6$, $w = 19.6$, and interactions = 47.

	r_1 (in.)	r_2 (in.)	σ_r (mS/m)	σ_{∞} (mS/m)
model	19.0	19.0	500.0	151.5
estimate	17.0	22.2	500.8	171.2

Invasion Model for Resistivity Logs

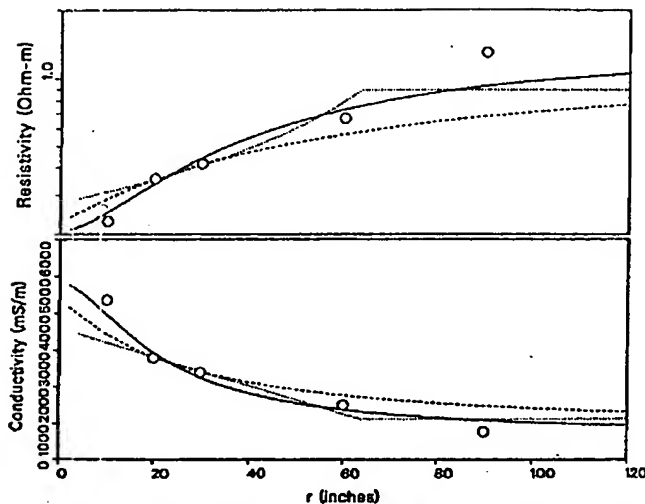


Figure 12: Thick-bed simulation where large dots are median curves, dotted line is model formation, dashed line is initial estimate, and solid line is DCLM estimate for $\chi^2_0 = 3.45 \times 10^0$, $c_N = 6.17 \times 10^3$, $N = 1.68$, $w = 22.0$, and iterations = 41.

	r_1 (in.)	r_2 (in.)	σ_i (mS/m)	σ_{xo} (mS/m)
model	4.0	64.0	1,124.0	3,448.0
estimate	4.0	48.1	734.2	4,836.0

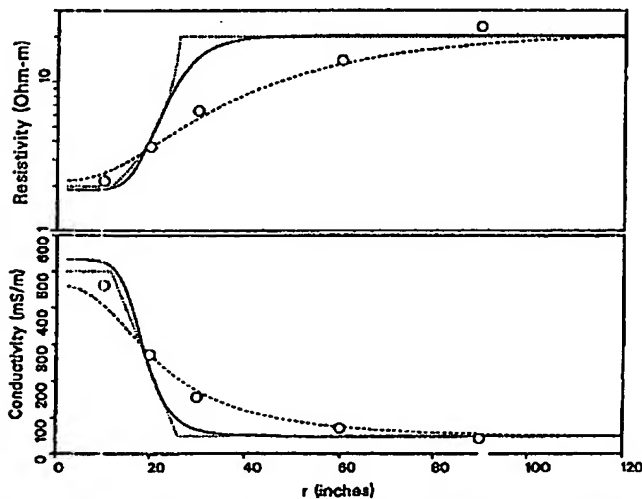


Figure 13: Thick-bed simulation where large dots are median curves, dotted line is model formation, dashed line is initial estimate, and solid line is DCLM estimate for $\chi^2_0 = 1.61 \times 10^{-1}$, $c_N = 7.54 \times 10^3$, $N = 6.6$, $w = 18.6$, and iterations = 22.

	r_1 (in.)	r_2 (in.)	σ_i (mS/m)	σ_{xo} (mS/m)
model	11.5	26.5	50.0	500.0
estimate	13.0	24.3	48.9	467.6

The five distinct open dots are the 10-, 20-, 30-, 60-, and 90-in. median-log input values. The dotted line is the input profile, the dashed line is the initial estimate, which is simply a four-parameter curve fit to the four median points, and the solid line is the DCLM estimate. These figures also give in table form the four parameters from equation (28), and both the input and estimated values of the two characteristic radii r_1 and r_2 defined by equation (25), σ_{xo} , and σ_i . The captions also include the χ^2_0 fit and condition number c_N of the DCLM matrix L' of equation (44). The quality of the solution is provided for the model parameters at each depth. Good solutions have small condition numbers, less than perhaps 10^4 , indicating numerical reliability. How well the model fits the data is more important and is measured by χ^2_0 from equation (40). When $\chi^2_0 < 2$, the fit is good.

In several instances, Figures 8–15 show that the median logs, although indicative of the shape of the profile, are not necessarily quantitatively correct because they are not point estimates but rather are center-weighted averages as their descriptor “median” suggests. Therefore, radial profiling schemes that do little more than curve fit to the median log values (as does the displayed dashed curve used for initializing DCLM) can have unacceptably large error.

One application of the shape of the invasion profile obtained with DCLM, which uses r_1 , r_2 , σ_{xo} , and σ_i , is to estimate the volume of mud filtrate per unit depth that has displaced the connate fluids. Figure 16 is a three-dimensional perspective of a simulated log through a finitely thick 20-ft bed with conductive invasion. The simulated data are computed by the semianalytic method (Chew et al., 1984). The exact model and estimated typical values for σ_i , σ_{xo} , r_1 , and r_2 are also included in table form for each of the three beds. Notice that in many of the shallow invasion results, the accuracy of the σ_i estimate is better than σ_{xo} . The method is designed to have better σ_i accuracy because the maximally flat-parameter model improves the sensitivity of the measurement to σ_i . The relatively less accurate σ_{xo} for shallow invasion cases is related to the radial response functions, which are small near the borehole (as can be seen from Figure 3). Nonetheless, the parametric processing improves the induction-based R_{xo} measurement.

No inversion study is complete without characterization of noise amplification, particularly when the processing is nonlinear and the linear steps in the iterations can have large condition numbers. Noise is added to four input curves in the following way. Noise of 10, 5, 2, and 1 mS/m standard deviation is added to the 10-, 20-, 30-, and 60-in. curves. The noise is computed by a Box-Muller transformation of uniformly distributed white noise. This transformation produces normally distributed random noise (Press et al., 1986, pp. 195–203). A large number, N_n , of such noise samples are added to the input curves,

Howard

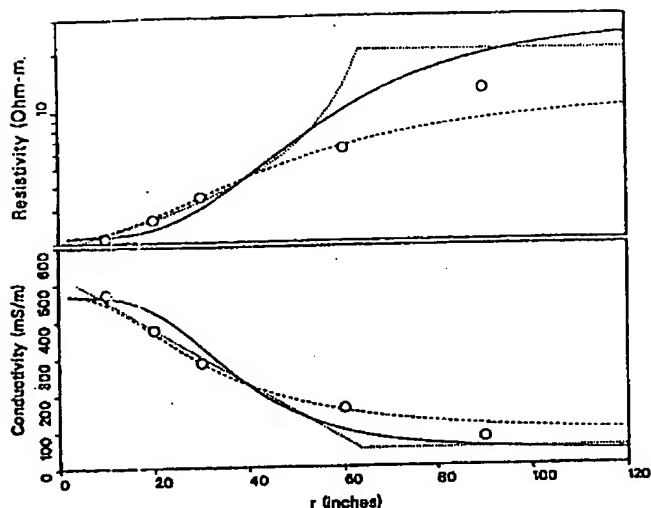


Figure 14: Thick-bed simulation where large dots are median curves, dotted line is model formation, dashed line is initial estimate, and solid line is DCLM estimate for $\chi^2 = 3.4 \times 10^{-1}$, $c_N = 2.24 \times 10^3$, $N = 3.6$, $w = 37.3$, and iterations = 151.

	r_1 (in.)	r_2 (in.)	σ_i (mS/m)	σ_{xo} (mS/m)
model	4.0	64.0	50.0	500.0
estimate	16.4	58.2	35.0	467.6

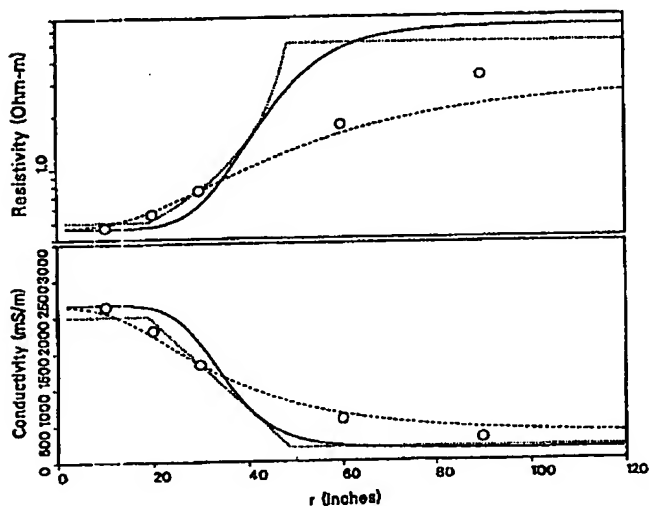


Figure 15: Thick-bed simulation where large dots are median curves, dotted line is model formation, dashed line is initial estimate, and solid line is DCLM estimate for $\chi^2 = 3.47 \times 10^{-1}$, $c_N = 1.76 \times 10^4$, $N = 6.5$, $w = 34.8$, and iterations = 24.

	r_1 (in.)	r_2 (in.)	σ_i (mS/m)	σ_{xo} (mS/m)
model	19.0	49.0	200.0	2,000.0
estimate	24.2	45.5	160.8	2,165.0

Table 1: Standard deviations of the four profile parameters from noise study. The additive noise is normally distributed noise with 10, 5, 2, and 1 mS/m standard deviation for, respectively, the 10-, 20-, 30-, and 60-in. curves.

Figure	σ_{xo} (mS/m)	σ_i (mS/m)	σ_w (in.)	σ_N (unitless)
8	56.0 (3.0)	3.0 (1.0)	0.18 (2.0)	2.3 (8.0)
9	5.0 (10.0)	2.0 (0.4)	0.17 (1.0)	0.6 (14.0)
10	10.0 (5.0)	4.0 (0.2)	0.21 (0.6)	0.02 (1.0)
11	11.0 (8.0)	0.2 (0)	0.08 (0.4)	1.2 (10.0)
12	58.0 (2.0)	140.0 (12.0)	1.2 (4.0)	2.4 (30.0)
13	3.0 (0.6)	1.6 (3.0)	0.18 (0.9)	6.1 (60.0)
14	10.0 (2.0)	6.7 (14.0)	1.1 (3.0)	0.5 (14.0)
15	10.0 (0.5)	1.8 (0.9)	0.13 (0.4)	0.8 (27.0)

¹ Numbers in parentheses are the ratio of the sample standard deviation estimate to actual value in percent. Results are based upon 100 experiments.

and the N_n resulting sets of parameters are saved. Sample statistical estimates of the resulting standard deviations for each of the four parameters are computed. The results of this statistical noise study for each of the examples in Figures 8–15 are summarized in Table 1. Each entry consists of the sample standard-deviation estimate, and in parentheses to the immediate right is the ratio of the sample standard-deviation estimate to actual value in percent (computed percent error results rounded to nearest 0.1%). Table 1 supports the conclusion that the inversion is quite robust for σ_i and w . As expected, the statistical variations of the shape parameters N and σ_{xo} are larger. N_n is 100.

Figures 8–16 illustrate typical accuracy of DCLM in known thick-bed environments. Figure 17 is a 100-ft field log recorded with the AIT. Each end of the interval is shale, and the center bed is an invaded water-saturated sandstone. Note that the DCLM-estimated R_i almost overlays the 60- and 90-in. curves, which is consistent with the rather shallow transition radius w that averages around 20 in. The R_{xo} estimate follows the 10-in. log but is more resistive and shows more activity. Based upon the quality indicators of condition number and the χ^2 fit, most of these narrow, more resistive R_{xo} zones are probably real. In most of this interval, the estimated apparent conductivity curves, $\hat{\sigma}_{ai}(m)$, fit the data σ_{ai} to several significant figures and have condition numbers, c_N , less than 10^1 . This increase confidence in the results. Two spikes at depths of 2,398 and 2,403 ft on the R_{xo} curve are probably not real because the c_N there are in excess of 10^6 . The ability of the parametric method to predict more thin resistive structure in R_{xo} than the shallow 10-in. curve results from the model-based extrapolation of the shape of the deeper transition region towards the well bore.

Invasion Model for Resistivity Logs

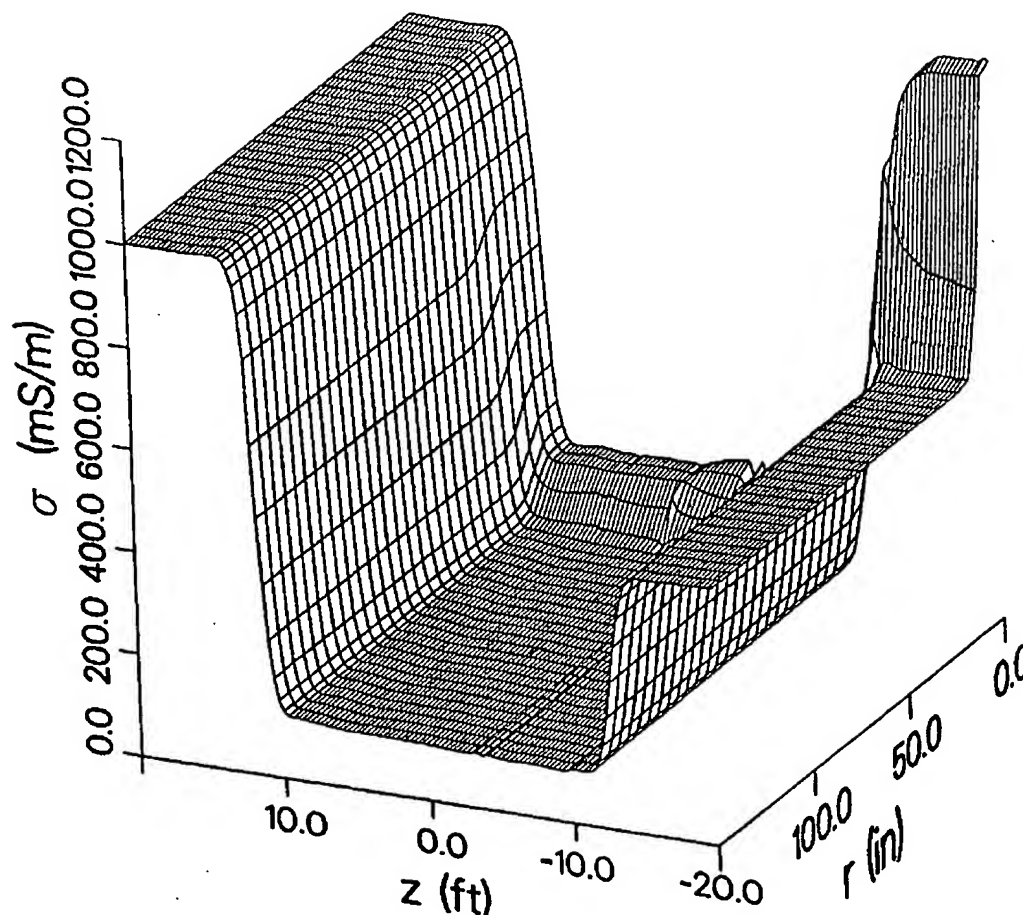


Figure 16. Step-invaded center bed of 20-ft thickness. Forward model is based on semianalytic method from Chew et al. (1984). In table, bed 1 is uninvaded where $z > 10$, and bed 2 is center bed where $-10 < z < 10$.

	r_1 (in.)	r_2 (in.)	σ_i (mS/m)	σ_{xo} (mS/m)
exact, bed 1	12.0	12.0	500.0	1,000.0
typical estimate	9.1	13.3	499.3	1,077.6
exact, bed 2	20.0	20.0	100.0	200.0
center estimate	8.4	16.7	105.0	222.0
exact, bed 3	0.0	0.0	1,000.0	1,000.0
typical estimate	0.0	0.0	1,001.0	999.0

CONCLUSIONS AND EXTENSIONS

This paper utilizes a parametric definition of a smooth radial invasion profile with a minimum number of parameters defining flushed, transition, and uninvaded regions. The parametric profiles are maximally flat in the flushed zone and in the limit of large N go over continuously to the traditional three-parameter σ_{xo} , σ_i , and D_i profile upon which the tornado-chart interpretation is based. Numerical results show that for shallow invasion, the accuracy of the σ_i estimate is better than σ_{xo} . The

maximally flat-parameter model improves the sensitivity of the measurement to σ_i . The parameters of the profile are shown by examples to be accurately estimated from median-log data. A new nonlinear algorithm (DCLM), coupled with the maximally flat-parametric invasion model, is key to extending the ability to deliver reliable R_i estimates in difficult invasion cases. The theory is developed in sufficient generality to estimate six or more parameters where annuli could in principle be detected. Induction data alone however are limited to resolving no

BLANK PAGE

Howard

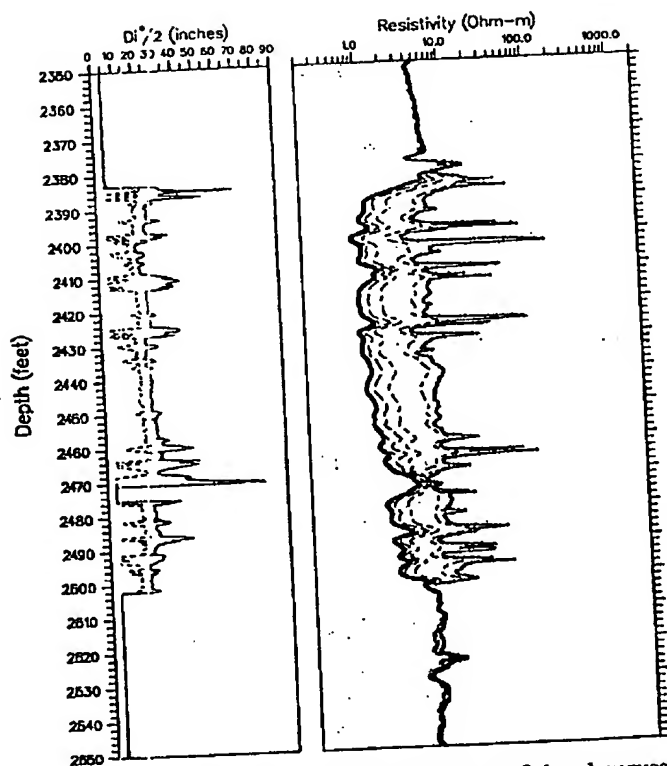


Figure 17: Field log with resistive invasion. Left-hand curves are radii of invasion r_1 (dashed) and r_2 (solid). The right-hand logs are, from left to right (in the direction of higher resistivity), the R curve, which is overlaying the 60- and 90-in. log curves, then the 30, 20, 10, and R_{xo} .

more than perhaps six parameters. Future work is planned to estimate more general nonmonotonic profiles and to determine conditions where the four-parameter method provides good R estimates in the presence of an annulus profile.

NOMENCLATURE

The following lists mathematical symbols, short definitions, and SI units. English units are used in numerical results. If no unit is provided, the quantity is a vector or matrix whose units are element dependent.

- c_v = condition number of L' matrix
- $C(m)$ = model constraint for $\chi^2(m)$, unitless
- D_i = diameter of invasion, m
- $f(\rho, w, \Lambda) = 1/[1 + (\rho/w)^\Lambda] = \text{Butterworth profile, unitless}$
- G_m^f = step response finite element matrix, unitless
- H = Hessian matrix in quadratic fit to χ^2
- j = induction-array index, unitless
- $J(\rho)$ = radial pseudo-response function, ohm
- $J_c(\rho)$ = radial cumulative pseudo-response function, ohm-m

- kHz = transmitter frequency in kiloHertz
- $K(\rho)$ = normalized radial response function, 1/m
- L = LM stabilized H matrix
- L'_m = LM matrix in terms of q_i parameters
- m = model parameter vector with elements m_i
- m_{new} = iteration update model vector m
- m_{old} = previous value of m_{new}
- m_{ok} = constraint function k th model parameter nominal value
- $m_1 = \hat{\sigma}_{xo}$ = estimate of σ_{xo} , S/m
- $m_2 = \hat{\sigma}_i$ = estimate of σ_i , S/m
- $m_3 = \hat{w}$ = estimate of w , m
- $m_4 = N$ = estimate of slope parameter N , unitless
- N = four-parameter slope parameter, unitless
- N_c = number of radial points used to determine profile, unitless
- $N_f = J_c(0)$ normalization for pseudo-response function, ohm-m
- N_p = number of model parameters, unitless
- N_R = number of radial pixels
- P_m^j = finite-element matrix, unitless
- $q_k = \sqrt{|m_k|}$ nonlinear change of variable to enforce positivity
- R_{mf} = mud-filtrate resistivity, ohm-m
- R_w = connate-water resistivity, ohm-m
- R_i = formation resistivity, ohm-m
- R_{xo} = flushed-zone resistivity, ohm-m
- $r_1 = w(1 - 2/N)$ = radius defining end of flushed zone, m
- $r_2 = w(1 + 2/N)$ = radius defining beginning of undisturbed zone, m
- $u(\rho - \rho_0)$ = step function = 1 for $\rho > \rho_0$, and zero otherwise
- w = four-parameter transition midpoint, m
- w_{im} = radial weight-function filter coefficients, unitless
- $\tilde{w}_f(\sigma_0)$ = apparent-conductivity focusing-filter weights, unitless
- z = borehole axial coordinate, m
- β = linear-term coefficient in quadratic approximation of χ^2
- β'_k = right-hand side of LM matrix equation in terms of q_i parameters
- $\delta(\rho - \rho_0)$ = impulse response function, 1/m
- δ_{nm} = Kronecker delta = 1 for $n = m$, and 0 otherwise, unitless
- $\delta_m = m_{new} - m_{old}$
- $\Delta_m = \rho_m - \rho_{m-1}$, m
- $\Delta\sigma$ = radial step change in conductivity, S/m
- γ = constant in quadratic χ^2 approximation, also dynamic constraint ratio, unitless
- λ = LM stabilizer and switch parameter, unitless
- $\Lambda_m(\rho)$ = triangular finite-element centered at $\rho = \rho_m$, unitless

March-April, 1992

The Log Analyst

Invasion Model for Resistivity Logs

- ϕ = azimuthal angle in borehole coordinates, radians
 r = radial coordinate, m
 ρ_m = radial coordinate at m th pixel, m
 σ_i = standard deviation of noise in i th log σ_{ai} , S/m
 $\sigma(\rho)$ = radial step conductivity profile, S/m
 $\sigma_{N_{c+1}}$ = dynamic-constraint factor determined by equation (45)
 $\sigma_4(\rho)$ = four-parameter radial conductivity profile, S/m
 $\sigma_6(\rho)$ = six-parameter radial conductivity profile, S/m
 σ_{xo} = flushed-zone conductivity, S/m
 σ_{an} = annulus conductivity, S/m
 σ_{ai} = i th median-log apparent conductivity, S/m
 σ_m = radial profile conductivity at radius $\rho = \rho_m$, S/m
 τ_{mk} = constraint function k th parameter tolerance
 σ_0 = a constant or background conductivity, S/m
 σ_a^j = j th raw induction array apparent conductivity, S/m
 σ_{a1}^j = j th step-response array apparent conductivity, S/m
 σ_{a2}^j = j th step-response array apparent conductivity, S/m
 σ_{a0}^j = j th induction array apparent conductivity for formation σ_0 , S/m
 $\hat{\sigma}_{ai}(m)$ = model estimate of log σ_{ai} , S/m
 σ_f = formation conductivity, S/m
 $\chi^2(m)$ = data fit parameter, unitless
 $\chi_0^2(m) = \chi^2(m) - C(m)$
 ∇ = gradient vector operator

ACKNOWLEDGEMENTS

I thank T. Broussard for his substantial contribution to testing and improving the algorithm and the ongoing task of commercial implementation of this method. Technical conversations with T. Barber, E. Head, R. Rosthal, and J. Tabanou were key to developing this method.

REFERENCES

- Allen, D., 1991, Invasion revisited: *Oilfield Review*, v. 3, no. 3, p. 10-23.
 Barber, T., and Rosthal, R., 1991, Using a multi-array induction tool to achieve high resolution logs with minimum environmental effects, SPE-22725, in SPE Annual Technical Conference and Exhibition Proceedings, v. omega, Formation Evaluation and Reservoir Geology: Society of Petroleum Engineers, p. 637-651.
 Broussard, S., 1989, The annulus effect: *Technical Review*, v. 37, no. 1, p. 41-47.
 Chew, W. C., Barone, S., Anderson, B., and Hennessy, C., 1984, Diffraction of axisymmetric waves in a borehole by bed boundary discontinuities: *Geophysics*, v. 53, p. 1577-1586.
 Dongarra, J. J., Moler, C. B., Bunch, J. R., and Stewart, G. W., 1979, *LINPACK user's guide*: Society of Industrial and Applied Mathematics, Philadelphia, Chapter 5.
 Grove, G. P., and Minerbo, G. N., 1991, An adaptive borehole correction scheme for array induction tools, Paper P, in Annual Logging Symposium Transactions: Society of Professional Well Log Analysts, 25 p.
 Howard, A. Q., Jr., and Chew, W. C., 1992, Electromagnetic borehole fields in a layered, dipping bed environment with invasion: *Geophysics*, v. 57, no. 3, p. 451-465.
 Howard, A. Q., Jr., Glass, C. E., Henry, D. B., N'Guessan, D. M., and Siemers, D. M., 1983, Wave diffusion tomography: U.S. Nuclear Regulatory Commission Report, NUREG/CR-3143, v. 4, 113 p.
 Hunka, J. F., Barber, T. D., Rosthal, R. A., Minerbo, G. N., Head, E. A., Howard, A. Q., Jr., Hazen, G. A., and Chandler, R. N., 1990, A new resistivity measurement system for deep formation imaging and high-resolution formation evaluation, SPE-20559, in Annual Technical Conference and Exhibition Proceedings, v. omega, Formation Evaluation and Reservoir Geology: Society of Petroleum Engineers, p. 295-307.
 Oppenheim, A. V., and Schaffer, R. W., 1975, *Digital signal processing*: Prentice-Hall, Englewood Cliffs, New Jersey, p. 219-220.
 Press, W. H., Flannery, B. P., Teukolsky, S. A., and Vetterling, W. T., 1986, *Numerical recipes*: Cambridge University Press, Cambridge, U.K., p. 521-528.
 Tittman, J., 1986, *Geophysical well logging*: Academic Press, Orlando, Florida, v. 24, excerpted from *Methods of experimental physics*, p. 88-90.
 Twomey, S., 1977, *Introduction to the mathematics of inversion in remote sensing and indirect measurements*: Elsevier, Amsterdam, Chapter 6, p. 122-149.
 Wait, J. R., 1984, General formulation of the induction logging problem for concentric layers about the borehole, in Special Issue on Electromagnetic Methods in Applied Geophysics: *IEEE Transactions on Geoscience and Remote Sensing*, v. GE-22, no. 1, p. 34-42.

APPENDIX

NORMALIZATION OF PSEUDO-RESPONSE FUNCTIONS

For completeness, the homogeneous background gain function $N(\sigma_0)$ for apparent conductivity as used in equation (8) is determined. In the most simple case of a magnetic dipole with coaxial coupling (coils are parallel, centered on the z axis, and in planes perpendicular to z axis), the received voltage v is from elementary theory (for a time dependence $e^{-i\omega t}$)

$$v = \kappa(1 - i\kappa r)e^{i\kappa r}, \quad (\text{A.1})$$

where

$$\kappa = 2i\omega\mu_0 m_R m_T I_0 / r^3,$$

$$r = |z_T - z_R|,$$

$$m_T = \pi \rho_T^2 N_T,$$

Howard

$$m_R = \pi \rho_R^2 N_R,$$

$$\mu_0 = 4\pi 10^{-7} \text{ H/m, and}$$

$$k = (i\omega\mu_0\sigma_0)^{1/2}.$$

The distances z and r are in cylindrical coordinates, N is number of turns, ω is the circular frequency, T and R subscripts denote transmitter and receiver, σ_0 is the background conductivity in S/m, and μ_0 is the permeability in H/m. To convert from voltage to apparent conductivity, the voltage v is divided by the sensitivity $\partial v / \partial \sigma|_{\sigma=0}$, where if v is computed numerically the evaluation is made at some finite but small conductivity where the relation between voltage and conductivity is linear, but the computation is accurate. Thus the dipole normalization is

$$N_d(\sigma_0) = \frac{\partial v / \partial \sigma|_{\sigma=\sigma_0}}{\partial v / \partial \sigma|_{\sigma=0}}. \quad (\text{A.2})$$

Use equation (A.1) to evaluate equation (A.2) resulting in

$$N_d(\sigma_0) = e^{ikr}. \quad (\text{A.3})$$

If the finite size of the loop antennas is important, the more general expression for the receiver voltage in the same geometry as equation (A.1) is

$$v = \kappa \int_0^\infty J_1(\lambda \rho_R) J_1(\lambda \rho_T) e^{i\lambda L} \frac{\lambda}{\beta} d\lambda, \quad (\text{A.4})$$

and

$$\beta = \sqrt{k^2 - \lambda^2},$$

$$\text{Im } \beta \geq 0,$$

$$L = |z_R - z_T|,$$

$$\kappa = -I_0 \omega \mu_0 m_R m_T / (\pi \rho_R \rho_T),$$

and J_1 is the Bessel function of the first kind of order 1. In the limit of small ρ_T and ρ_R , equation (A.4) becomes equal to equation (A.1). The resulting normalization function in this case is much more complicated. Nonetheless, it can be shown that in this more general case the normalization is exactly given by

$$N(\sigma_0) = \frac{-i \int_0^{\pi/2} (1 - 2 \sin^2 \theta) e^{ikR} d\theta}{k \int_0^{\pi/2} (1 - 2 \sin^2 \theta) R d\theta}. \quad (\text{A.5})$$

where

$$R = \sqrt{\alpha + \beta} \sqrt{1 - \gamma^2 \sin^2 \theta},$$

$$\alpha = L^2 + \rho_R^2 + \rho_T^2,$$

$$\beta = 2\rho_R \rho_T,$$

$$\gamma = 2\beta / (\alpha + \beta).$$

In the limit of small loops, equation (A.5) goes to the dipole result (A.3). Multi-coil sonde normalizations are simple linear combinations of these results.

ABOUT THE AUTHOR

Allen Q. Howard, Jr. obtained a Ph.D. in physics from the University of Colorado in 1972. His thesis advisor was Prof. James R. Wait. From 1965 to 1974, he was a member of the technical staff of the Institute of Telecommunication Sciences, U.S. Department of Commerce in Boulder, Colorado. While there, he developed mathematical models for terrestrial radio wave propagation. In 1973, he was a visiting Professor of Electrical Engineering at the Catholic University in Rio de Janeiro, Brazil. In 1974, he joined the Department of Electrical Engineering at the University of Arizona, Tucson, as an Assistant Professor. In 1977, he was promoted to Associate Professor. In 1982, he took sabbatical leave with Britoil in Glasgow, Scotland, to work on induction logging theory. In 1985, he joined Schlumberger Well Services in Houston, Texas. Mr. Howard is a Fellow of IEEE, member of Electromagnetics Academy, Who's Who in Electromagnetics, Commissions B and F of the International Scientific Radio Union (URSI), and SEG. He is associate editor for Electromagnetic Subsurface Remote Sensing for the IEEE Transactions on Geoscience and Remote Sensing. Mr. Howard is URSI Technical Program Chairman for the IEEE-IGARSS and URSI 1992 meeting in Houston. His technical interests are geophysical applications of electromagnetic theory and signal processing.

**This Page is Inserted by IFW Indexing and Scanning
Operations and is not part of the Official Record**

BEST AVAILABLE IMAGES

Defective images within this document are accurate representations of the original documents submitted by the applicant.

Defects in the images include but are not limited to the items checked:

- ☐ BLACK BORDERS
- ☐ IMAGE CUT OFF AT TOP, BOTTOM OR SIDES
- ☐ FADED TEXT OR DRAWING
- ☐ BLURRED OR ILLEGIBLE TEXT OR DRAWING
- ☐ SKEWED/SLANTED IMAGES
- ☐ COLOR OR BLACK AND WHITE PHOTOGRAPHS
- ☐ GRAY SCALE DOCUMENTS
- ☒ LINES OR MARKS ON ORIGINAL DOCUMENT
- ☐ REFERENCE(S) OR EXHIBIT(S) SUBMITTED ARE POOR QUALITY
- ☐ OTHER: _____

IMAGES ARE BEST AVAILABLE COPY.

As rescanning these documents will not correct the image problems checked, please do not report these problems to the IFW Image Problem Mailbox.